ARL-TR-9980 • SEP 2024

Development of Al–Ce–Mg–Zn-based Alloys

by Taylor W Cain and Jon-Erik Mogonye

DISTRIBUTION STATEMENT A. Approved for public release: distribution unlimited.

NOTICES

Disclaimers

ARL-TR-9980 ● SEP 2024

Development of Al–Ce–Mg–Zn-based Alloys

Taylor W Cain and Jon-Erik Mogonye
DEVCOM Army Research Laboratory

REPORT DOCUMENTATION PAGE

1. REPORT DATE	2. REPORT TYPE	3. DATES COVERED: START DATE	END DATE
September 2024	Technical Report	October 2020	December 2023

4. TITLE AND SUBTITLE
Development of Al–Ce–Mg–Zn-based Alloys

5a. CONTRACT NUMBER	5b. GRANT NUMBER	5c. PROGRAM ELEMENT NUMBER
5d. PROJECT NUMBER	**5e. TASK NUMBER**	**5f. WORK UNIT NUMBER**

6. AUTHOR(S)
Taylor W Cain and Jon-Erik Mogonye

7. PERFORMING ORGANIZATION NAME(S) AND ADDRESS(ES)	8. PERFORMING ORGANIZATION REPORT NUMBER
DEVCOM Army Research Laboratory ATTN: FCDD-RLA-VA Aberdeen Proving Ground, MD 21005	ARL-TR-9980

9. SPONSORING/MONITORING AGENCY NAME(S) AND ADDRESS(ES)	10. SPONSOR/MONITOR'S ACRONYM(S)	11. SPONSOR/MONITOR'S REPORT NUMBER(S)

12. DISTRIBUTION/AVAILABILITY STATEMENT
DISTRIBUTION STATEMENT A. Approved for public release: distribution unlimited.

13. SUPPLEMENTARY NOTES
ORCIDs: Taylor W Cain, 0000-0002-6621-914X; Jon-Erik Mogonye, 0000-0002-7508-083X

14. ABSTRACT
Al–Ce–Mg–Zn based hypoeutectic alloys were investigated for their efficacy in coarsening resistant high temperature applications. Nine unique compositions were investigated via various heat treatments and casting methods including button melting (25 g), small rod casting (300 g), and wedge casting (1150 g) to evaluate the mechanical properties and coarsening resistance. Results showed a large hardening response owing to precipitation of the τ-$Mg_{32}(Al,Zn)_{49}$ phase but rapid overaging was observed above 200 °C. Furthermore, the τ-$Mg_{32}(Al,Zn)_{49}$ phase did not show coarsening resistance at temperature above 200 °C as desired. As such, industrialization is suggested for applications below 100 °C.

15. SUBJECT TERMS
aluminum casting, aluminum alloy, eutectic alloy, aluminum cerium alloy, aluminum cerium magnesium zinc alloy, T-phase, Mechanical Sciences, Sciences of Extreme Materials

16. SECURITY CLASSIFICATION OF: a. REPORT	b. ABSTRACT	C. THIS PAGE	17. LIMITATION OF ABSTRACT	18. NUMBER OF PAGES
UNCLASSIFIED	UNCLASSIFIED	UNCLASSIFIED	UU	35

19a. NAME OF RESPONSIBLE PERSON	19b. PHONE NUMBER *(Include area code)*
Jon-Erik Mogonye	(410) 278-9545

STANDARD FORM 298 (REV. 5/2020)
Prescribed by ANSI Std. Z39.18

Contents

List of Figures

List of Tables

Acknowledgments

We would like to thank Mr Benjamin Serratos for help with metallographic preparation and scanning electron microscopy as well as Mr Christopher Carangelo for performing tensile testing for this report.

1. Introduction

Aluminum–cerium (Al–Ce)-based eutectic alloys have recently been identified as a promising new class of alloys to replace legacy Al–Cu and Al–Si-based eutectic alloys in a variety of applications.[1,2] These alloys are currently being investigated through both traditional casting and various additive-manufacturing-based techniques. The Al–Ce system forms a eutectic near 11 wt% Ce, which follows the solidification reaction L → α-Al + $Al_{11}Ce_3$. The $Al_{11}Ce_3$ phase has shown higher coarsening resistance to eutectic Al_2Cu in Al–Cu-based casting alloys and ß-Si in Al–Si-based casting alloys,[1] which makes Al–Ce alloys very attractive for high-temperature applications where Al alloys are required.

Most research on Al–Ce-based alloys occurred within the last 5 years where the Al–Ce–Mg,[1–6] Al–Ce–Ni,[7–9] Al–Ce–Mn,[10–15] and Al–Ce–Ni–Mn[16–22] systems received the broadest amount of attention. However, there are no published reports on the solidification behavior and mechanical properties of Al–Ce–Mg–Zn-based alloys.

The goal of this research was to study the effect of Mg and Zn content on the microstructural and mechanical property response. Alloys were first produced as small buttons on the order of 20–25 g and characterized by scanning electron microscopy (SEM), X-ray diffraction (XRD), and hardness measurements to identify promising compositions for scaled-up production testing. Down-selected alloys were scaled up and produced as either cast rods (≈300 g) or wedge casting (≈1400 g) to study the effects of heat treatment and solidification rates.

2. Methods

2.1 Fabrication of Button Alloys

Production of button alloys was completed by using 99.9% pure Mg (US Magnesium LLC), 99.99% pure Zn (Alfa Aesar), and an Al-10 wt% Ce master alloy (Eck Industries). Buttons were first produced to investigate the effect of Ce. The targeted composition of these alloys was Al–4Mg–4Zn–xCe where x = 3, 5, 7, and 9 wt%. A second, larger matrix of buttons was made with a constant Ce concentration of 7 wt% while varying Mg and Zn. These compositions can be found in Table 1.

Table 1 Target composition of button alloys investigated

Alloy name	Al (wt%)	Ce (wt%)	Mg (wt%)	Zn (wt%)
CMZ722	Bal.	7	2	2
CMZ724	Bal.	7	2	4
CMZ726	Bal.	7	2	6
CMZ742	Bal.	7	4	2
CMZ744	Bal.	7	4	4
CMZ746	Bal.	7	4	6
CMZ762	Bal.	7	6	2
CMZ764	Bal.	7	6	4

The appropriate amount of material for approximately 20 g of charge was placed within a 35-mm-diameter, high-purity graphite crucible and loaded into a 25-kW vacuum induction melting (VIM) furnace with an output frequency of 30–80 kHz. Prior to melting, the furnace was purged under vacuum and backfilled three times with ultra-pure He (99.999%) to remove oxygen from the chamber. The graphite crucible was heated under a positive flow of He gas to a temperature of 750 °C. Once molten, the alloys were allowed to mix for 10 min using mechanical shaking and then allowed to solidify via furnace cooling. Furnace cooling under these conditions produces a solidification rate of approximately 0.4 °C/s, which is similar to that of a sand casting.[23]

2.2 Fabrication of Rod and Wedge Castings

Cast rods were produced by melting approximately 300 g of total charge in a graphite crucible using an Indutherm VTC 800 V/Ti vacuum induction melting furnace. Melting was performed after purging the melt chamber under vacuum and backfilling with high-purity Ar (99.999%) one time prior to heating and once while heating, to lower oxygen impurities in the melt chamber. The alloy was melted to a temperature of 750 °C and held for 10 min, stirring every 5 min; slag was removed prior to casting. The alloy melt was cast into a 35-mm-diameter × 75-mm-tall graphite crucible, which was embedded in olivine sand and preheated to a temperature of 200 °C. Wedge castings were produced under the same melting conditions but cast into a BN-coated Cu mold preheated at 400 °C. The geometry of the wedge mold is found in Fig. 1.

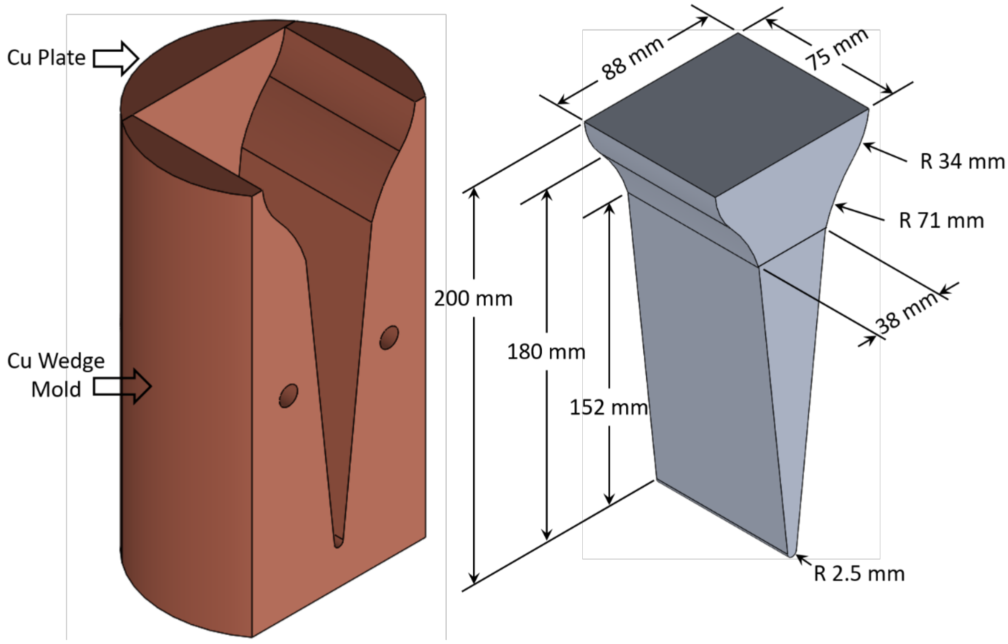

Fig. 1 Drawing of the Cu wedge mold and resulting wedge geometry. The wedge has an approximate volume of 425 cm^3.

2.3 Characterization of Cast Alloys

Alloy specimens used for characterization by SEM and hardness were cold mounted in epoxy and ground using successive SiC grinding papers up to 1200 grit CAMI finish. Final polishing used 1- and 0.25-µm water-based diamond suspensions and 0.05-µm colloidal silica. SEM was performed using a Hitachi SU3500 equipped with a Bruker QUANTAX energy-dispersive spectroscopy (EDS) detector. Hardness was measured using either Rockwell B or micro-Vickers testing. A Mitutoyo HM-200 Vickers hardness tester was used with a 0.3-kgf load with a 5-s load time, 10-s dwell time, and 5-s unload time. XRD was measured using a Bruker D2 phaser, with a Co X-ray source (K_α λ = 1.7902 Å). Experiments were performed in the Bragg–Brentano geometry with a 2θ scan range of either 15–90° or 15–120°, a step size of 0.02°, and a dwell of 1 s per step.

3. Results and Discussion

3.1 Button Melt Matrices

3.1.1 Al–xCe–4Mg–4Zn (x = 3, 5, 7, 9)

Representative backscattered electron (BSE) images for each alloy button in the as-solidified state are shown in Fig. 2. Three phases can be seen from these images: 1) the α-Al matrix as the dark background, 2) medium-brightness particles with a divorced eutectic phase (DEP) morphology, and 3) a bright phase in the form of a Chinese-script-type morphology typically associated with the $Al_{11}Ce_3$ phase. The medium-brightness phase was identified to be the τ-$Mg_{32}(Al,Zn)_{49}$ phase via XRD (Fig. 3). From initial visual inspection, the volume fraction of the $Al_{11}Ce_3$ phase appeared to increase with increasing Ce concentration, as would be expected for this system where CMZ944 appeared to be near the eutectic composition and all other compositions were hypoeutectic. The formation of a blocky $Al_{11}Ce_3$ phase can be found in all alloys as shown by the arrows in Fig. 2 and increases with increasing Ce. This trend of increasing $Al_{11}Ce_3$ phase formation was further confirmed using quantitative image analysis on BSE images that were segmented using the Labkit intuitive pixel classification tool within Fiji (Fig. 4). Interestingly, the τ-$Mg_{32}(Al,Zn)_{49}$ phase area fraction decreased with increasing Ce. This is likely due to the reduced fraction of α-Al dendrites from which divorced eutectic τ-$Mg_{32}(Al,Zn)_{49}$ phase forms as the last solid between dendrite arms. Despite these trends in microstructure, the hardness measured on each alloy in the as-solidified state were all approximately 50 Rockwell B hardness (HRB) within scatter, which indicates that the solid solution-strengthening contribution of Mg and Zn in these alloys and any precipitation hardening are the dominant strengthening mechanisms (Fig. 5). Furthermore, all alloys exhibited a similar hardness to an A356.0 button that had been peak aged using a T6 heat treatment. To further elucidate the effect of Mg and Zn contents on the hardening response of Al–Ce–Mg–Zn alloys, additional buttons at constant Ce but varying Mg and Zn were made. For these buttons, 7 wt% Ce was chosen due to being hypoeutectic.

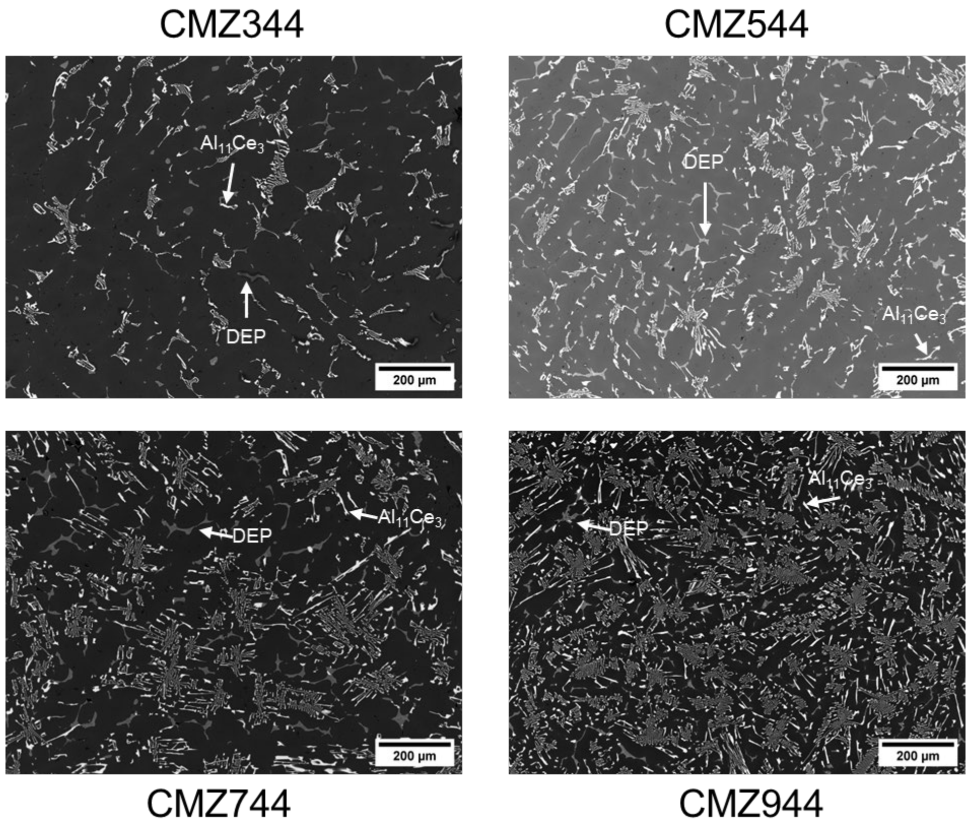

Fig. 2 Representative BSE images of Al–xCe–4Mg–4Zn alloy buttons in the as-solidified form. The DEP and primary $Al_{11}Ce_3$ phases are highlighted by arrows in each image.

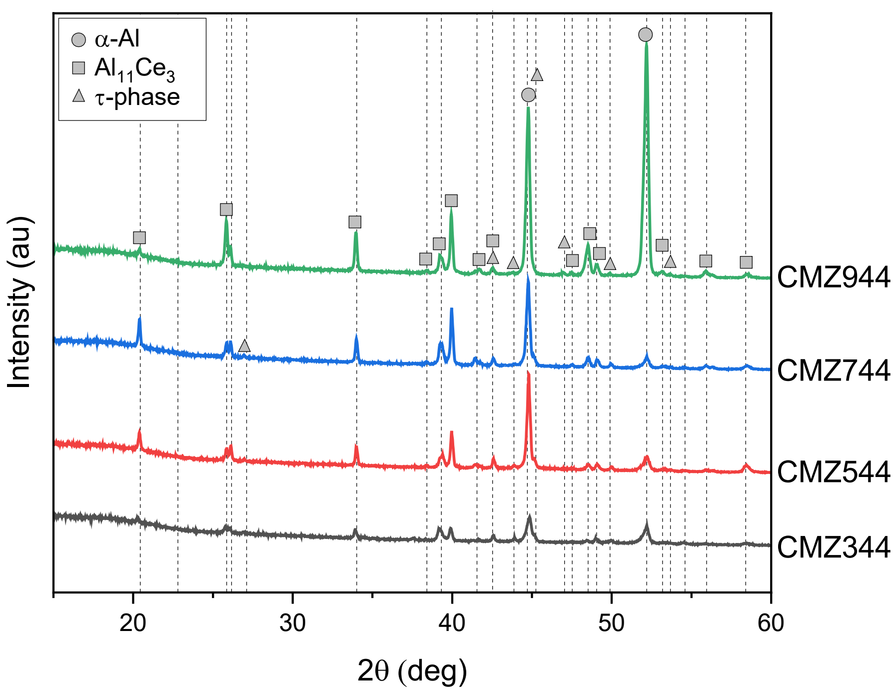

Fig. 3 Powder XRD patterns for Al–xCe–4Mg–4Zn alloy buttons in the as-solidified condition

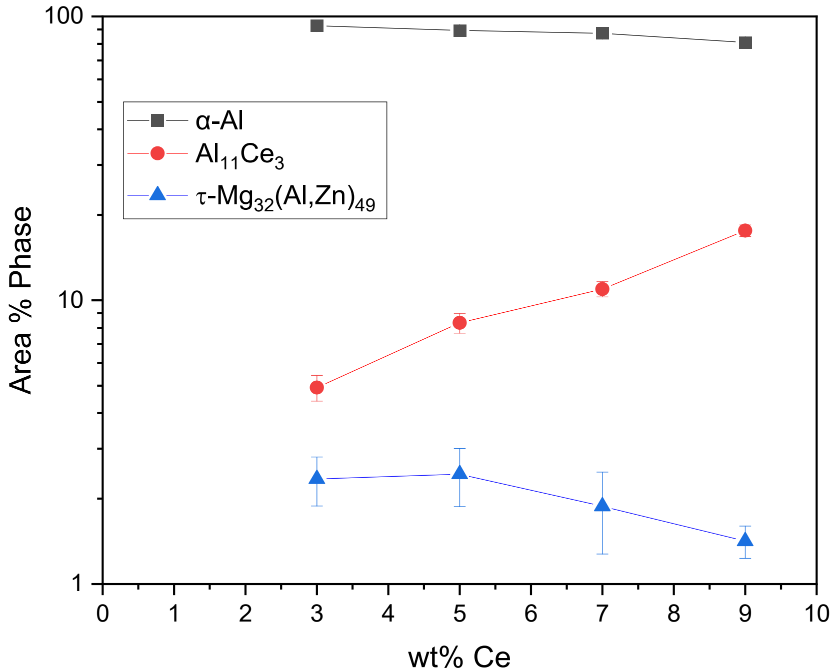

Fig. 4 Area percentage of phases present in Al–xCe–4Mg–4Zn alloy buttons in the as-solidified state

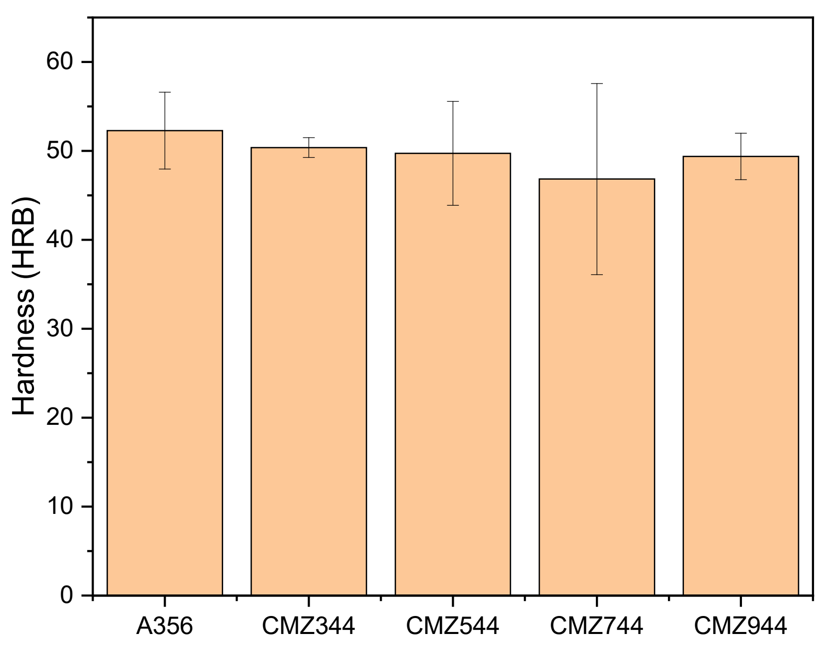

Fig. 5 Hardness of Al–xCe–4Mg–4Zn buttons in the as-solidified form compared to A356.0-T6 button

3.1.2 Al–7Ce–xMg–yZn Alloy Buttons

Representative BSE images of Al–7Ce–xMg–yZn alloys is shown in Fig. 6 for buttons in the as-solidified state. The $Al_{11}Ce_3$ phase is the dominant secondary phase present in all alloys given by the bright contrast and Chinese script morphology. Primary $Al_{11}Ce_3$ formation can also be detected as the total concentration of Mg and Zn additions increases—as observed only for CMZ746 with a large, blocky $Al_{11}Ce_3$ phase in the middle of the BSE image. There is also a medium-contrast phase that forms as a divorced eutectic when the Mg and Zn concentrations increase. Powder XRD patterns for these alloys show that the medium-brightness phase is either τ-$Mg_{32}(Al,Zn)_{49}$ or an Al_2CeZn_2 phase (Fig. 7). The Al_2CeZn_2 phase was only present in XRD patterns for alloys with 6 wt% Zn while τ-$Mg_{32}(Al,Zn)_{49}$ was present in alloys except CMZ722, CMZ724, and CMZ742. However, BSE images clearly show the presence of the medium-contrast phase indicating a low-volume fraction of this phase. Quantitative image analysis of BSE images is shown in Fig. 8 and provides the breakdown of phase fraction for α-Al, $Al_{11}Ce_3$, and all other phases. Some interesting trends were observed for the different series of cast alloys with the fraction of α-Al increasing for Al–7Ce–2Mg–xZn with an increase in Zn concentration while it decreased for Al–7Ce–4Mg–xZn and Al–7Ce–6Mg–xZn. Meanwhile, the fraction of $Al_{11}Ce_3$ decreased greatly with increasing Zn for Al–7Ce–2Mg–xZn and was relatively constant for Al–7Ce–4Mg–xZn and Al–7Ce–6Mg–xZn. Additionally, the fraction of $Al_{11}Ce_3$ decreased with increasing Mg concentration at constant Zn. The opposite was true for the fraction of other phases present with the fraction of other phases increasing with both increasing Mg and Zn indicating that Mg and Zn are primary element formers in the other phases present.

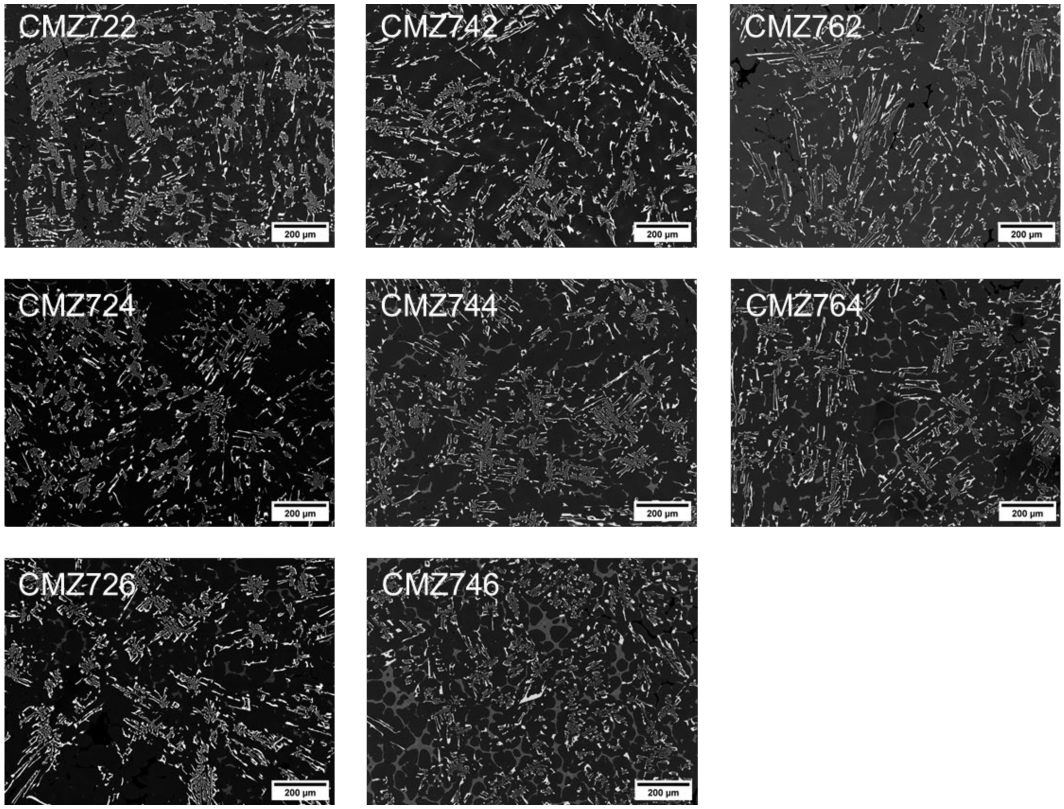

Fig. 6 Representative BSE images of Al–7Ce–xMg–yZn alloy buttons in the as-solidified form

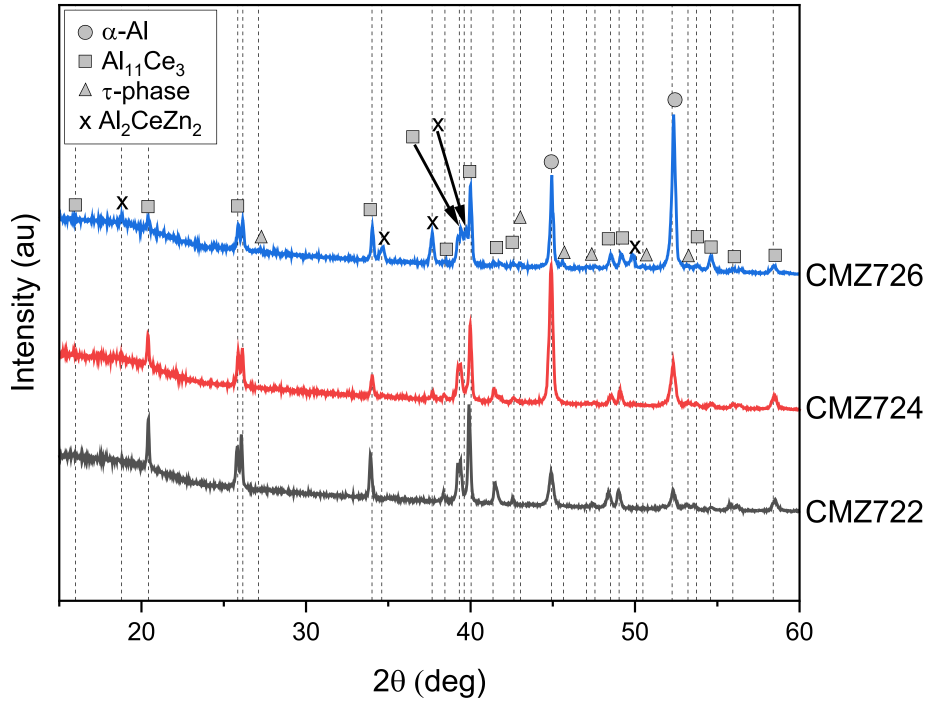

(a)

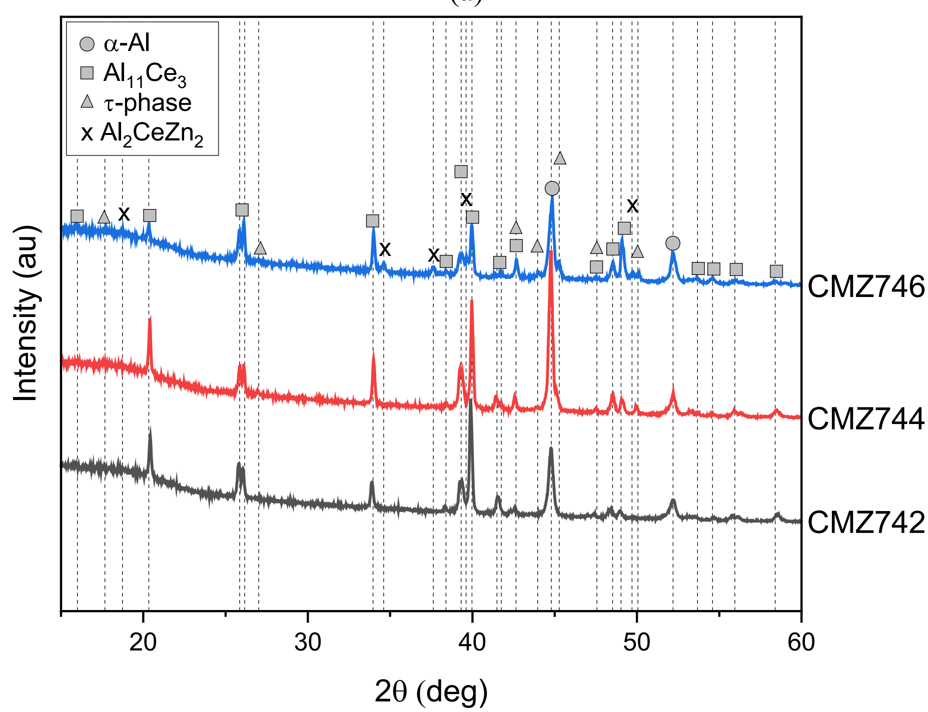

(b)

Fig. 7 Powder XRD patterns for as-solidified (a) CMZ722, CMZ724, CMZ726, (b) CMZ742, CMZ744, CMZ746, and (c) CMZ762 and CMZ764

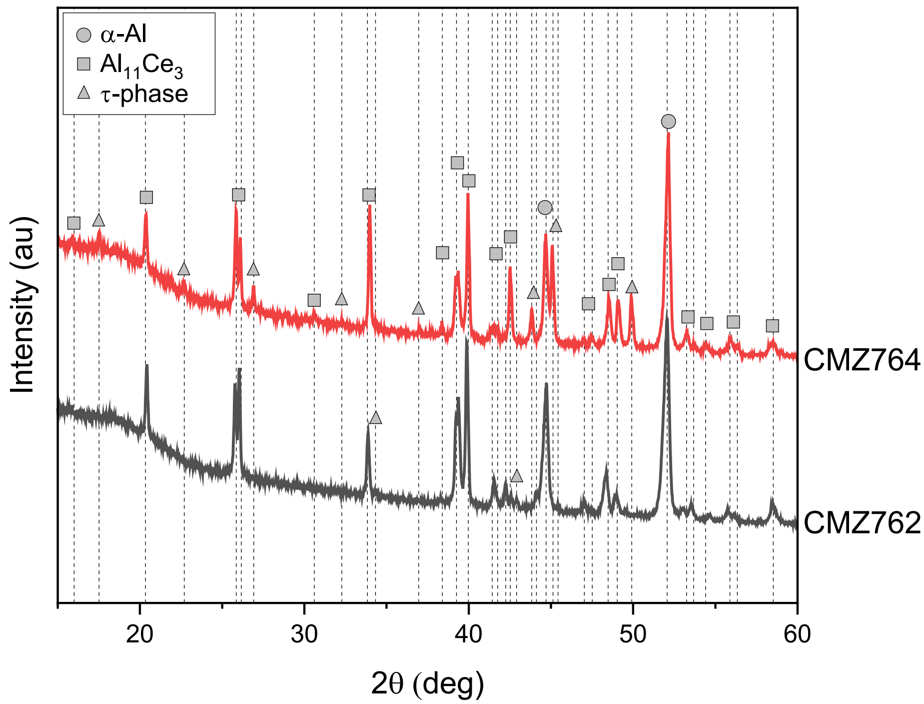

(c)

Fig. 7 Powder XRD patterns for as-solidified (a) CMZ722, CMZ724, CMZ726, (b) CMZ742, CMZ744, CMZ746, and (c) CMZ762 and CMZ764 (continued)

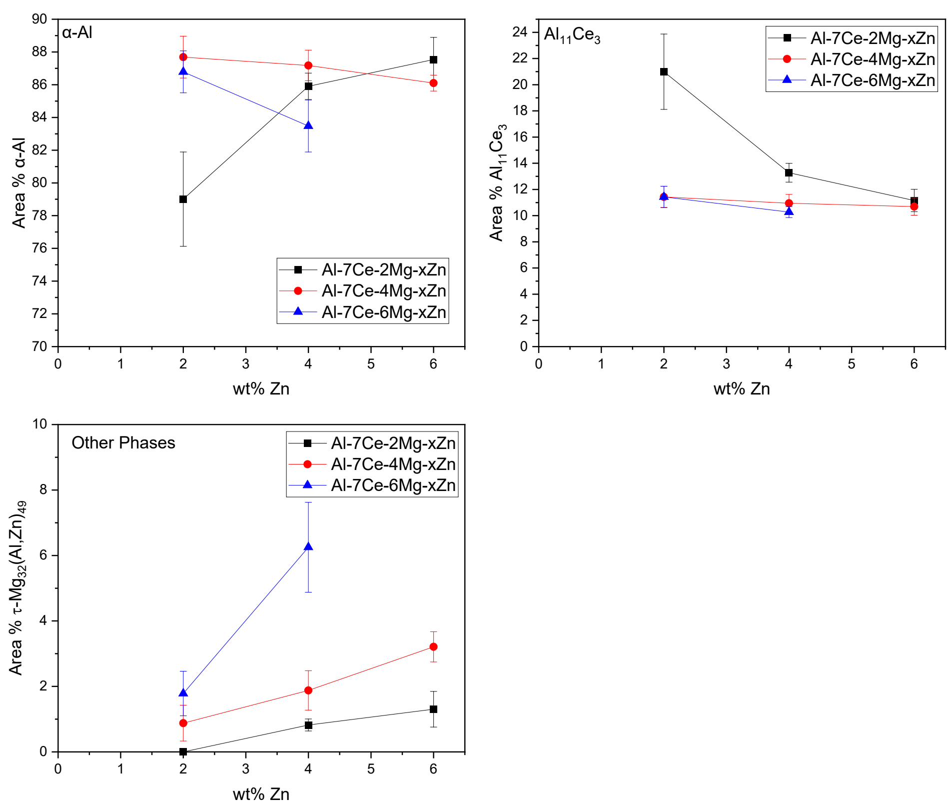

Fig. 8 Area percentage of phases present in Al–7Ce–xMg–yZn as-solidified buttons. Values were determined by quantitative image analysis in Fiji.

Al–7Ce–xMg–yZn buttons were subjected to a homogenization treatment of 432 °C for 6 h to explore the solid solution-strengthening effects of Mg and Zn. Figure 9 shows an example of the microstructures before and after homogenization treatment for CMZ764. Clear homogenization of the Mg elemental signal was seen via EDS mapping given the uniform signal intensity within the α-Al matrix in the homogenized state as compared to the localized signal near the Mg- and Zn-rich precipitates in the as-solidified state. This was the greatest change observed as there was no indication of any dissolution of the Mg–Zn-rich phase because the homogenization effect and the signal intensity for Zn in the α-Al matrix was low in both conditions. Interestingly, there is some Zn signal associated with the Ce-rich phase regions indicating some solubility of Zn in $Al_{11}Ce_3$.

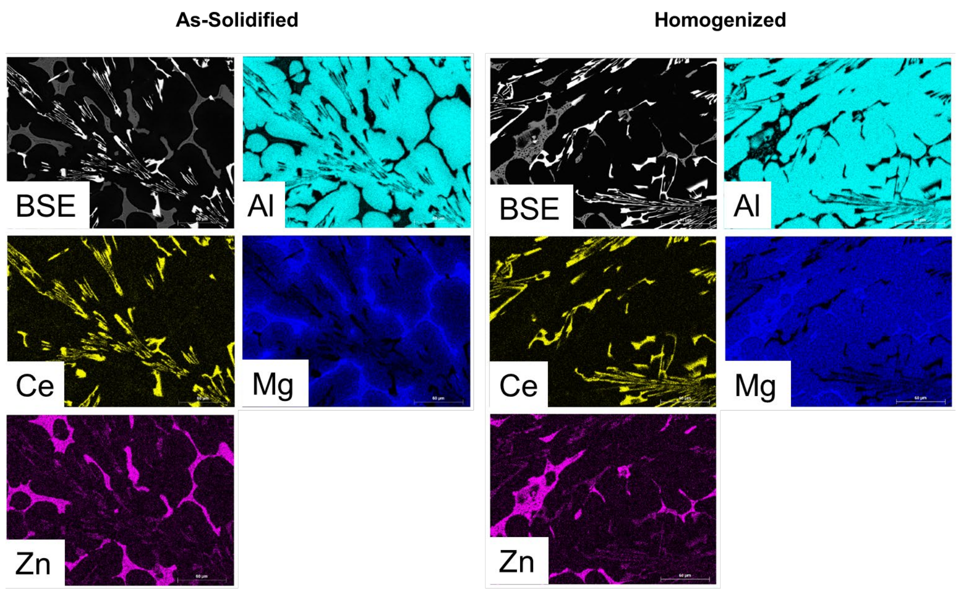

Fig. 9 Representative BSE image with corresponding EDS mapping of the Al, Ce, Mg, and Zn elemental signals in the as-cast state and after a homogenization treatment of 432 °C for 6 h for CMZ764

Hardness measurements in both the as-solidified and homogenized states were performed with both Rockwell B and Vickers microhardness. The results for HRB (Fig. 10) revealed increasing hardness with both increasing Mg and Zn concentration with the highest hardness skewing toward Zn-rich compositions. This trend was also shown after homogenization except that greater hardness values skewed toward Mg-rich compositions. Furthermore, the hardness of Mg-rich compositions increased after homogenization as shown in Fig. 10c using Eq. 1:

$$\%\,Hardness\ retention = \left(1 + \frac{H_H - H_S}{H_S}\right) \times 100\%\ , \tag{1}$$

where H_H is the homogenized hardness and H_S is the as-solidified hardness. This indicated that Mg experienced a greater effect due to the homogenization treatment, which would be expected from the EDS mapping in Fig. 9, while the hardness of Zn-rich compositions decreased due to partitioning to the Al–Ce rich phase. The effects of homogenization on the hardness of the α-Al matrix and the eutectic colonies were investigated with Vickers microhardness testing and are shown in Figs. 11 and 12, respectively. These figures revealed a similar trend to the HRB where high hardness is observed for both the matrix and eutectic phase in the Mg- and Zn-rich compositions, with the hardness decreasing for Zn-rich compositions after homogenization while Mg-rich compositions increased in hardness. Interestingly, the hardness measured for the matrix and eutectic colonies were like each other at each composition, indicating that the primary strength results from the solid solution-strengthening effect and any nano precipitates within the matrix from any natural aging.

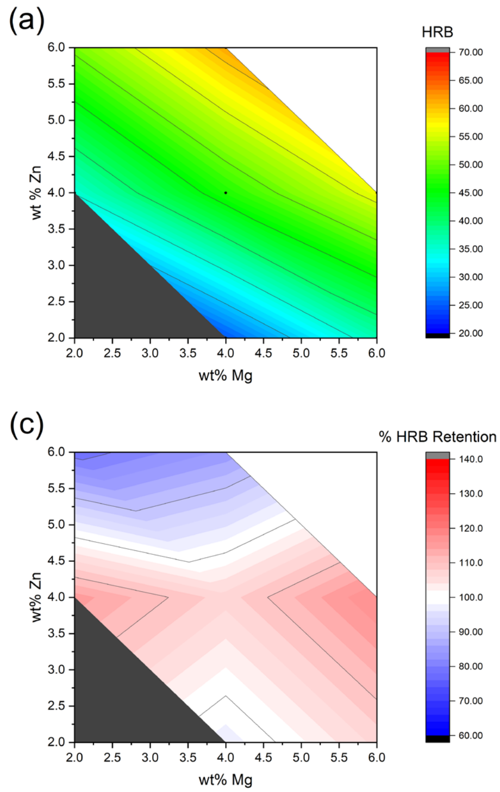

Fig. 10 The average HRB for the α-Al matrix phase of Al–7Ce–xMg–yZn buttons in the (a) as-solidified form, (b) after homogenization at 432 °C for 6 h, and (c) as a function of hardness retention. Note that the hardness of CMZ722 was too low to be measured on the Rockwell B scale.

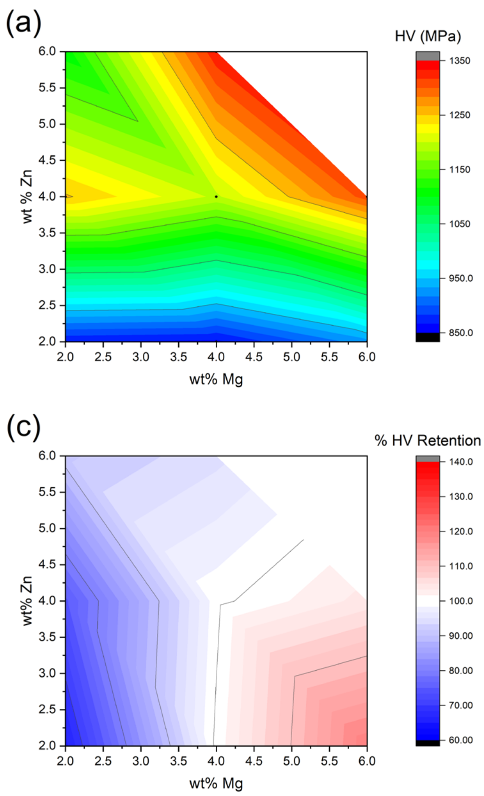

Fig. 11 The average Vickers hardness for the α-Al matrix phase of Al–7Ce–xMg–yZn buttons in the (a) as-solidified form, (b) after homogenization at 432 °C for 6 h, and (c) as a function of hardness retention

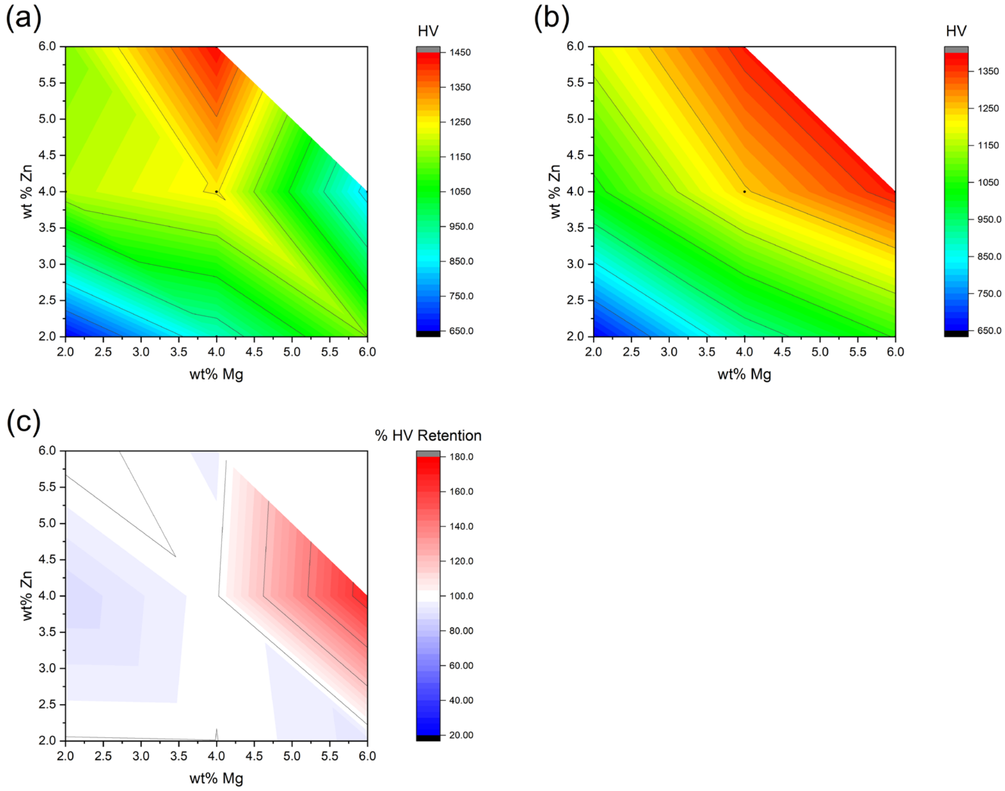

Fig. 12 The average Vickers hardness for the eutectic phase colonies of Al–7Ce–xMg–yZn buttons in the (a) as-solidified form, (b) after homogenization at 432 °C for 6 h, and (c) as a function of hardness retention. Isochronal hardness of (a) CMZ764 and CMZ975 in Rockwell B and (b) CMZ764 in Vickers microhardness of the α-Al matrix and eutectic phase colonies under a load of 0.3 kgf.

3.2 Rod Melts

Small-scale rods were cast for CMZ764 and CMZ975 to further investigate the effects of heat treatment on the hardness evolution. CMZ975 was chosen to increase the fraction of $Al_{11}Ce_3$ phase fraction while maintaining a similar ratio of Ce:Mg:Zn. Rods were sectioned into 1/4-inch-thick slices that were cut in half to produce a half-circle-shaped sample in the planar section. Samples for the cut rods were subjected to various heat treatments to assess age hardenability and thermal stability. Single-axis equilibrium calculations made in Thermo-Calc (TCAL7 database) (Fig. 13) show that the τ-$Mg_{32}(Al,Zn)_{49}$ phase is stable up to 430 °C for CMZ764 and 458 °C for CMZ975 while the liquidus for CMZ764 is 500 °C and 458 °C for CMZ975, indicating that CMZ975 cannot be solution treated. Thus, heat treatments were only performed from the as-cast state.

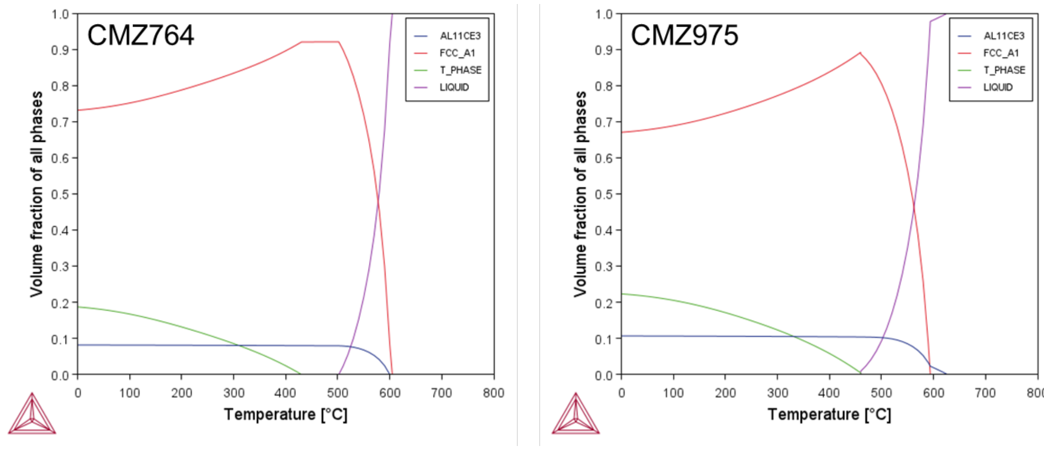

Fig. 13 Volume fraction of all equilibrium phases as a function of temperature for CMZ764 and CMZ975 produced by Thermo-Calc with the TCAL7 database

3.2.1 Isochronal Aging

Isochronal aging was performed between 150 and 400 °C at 50 °C intervals for 2 h. Prior to isochronal aging, samples were solution treated at 485 °C for 2 h followed by water quenching. The hardness measured by Rockwell B for both CMZ764 and CMZ975 (Fig. 14a) revealed similar hardness values for both alloys at each temperature. The hardness increased to a peak value at 200 °C and rapidly decreased to the final temperature of 400 °C. The peak HRB of CMZ764 was approximately 41% greater than the as-cast hardness, while the peak HRB of CMZ975 was approximately 36% greater than that of the as-cast hardness. This indicates excellent age hardenability of the CMZ alloy system. A comparison of the matrix hardness to the hardness of eutectic colonies (Fig. 14b) for CMZ764 revealed a similar hardness value of the matrix to the eutectic colonies as was observed for Al-7Ce-xMg-yZn buttons. The measurement for Vickers hardness also showed the same trend as the isochronal measurements of Rockwell B with a peak hardness at 200 °C with approximately 32% increase in hardness compared to the as-cast state for both the α-Al matrix and the eutectic phase colonies.

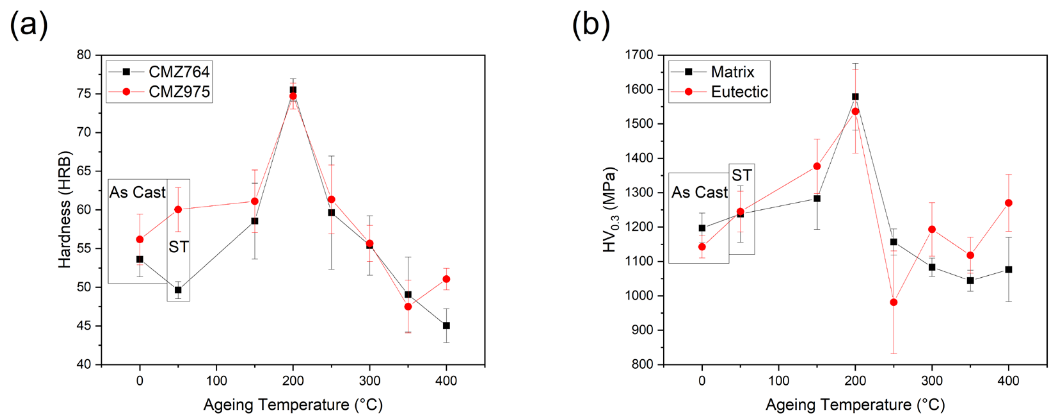

Fig. 14 Isochronal hardness of (a) CMZ764 and CMZ975 in Rockwell B and (b) CMZ764 in Vickers microhardness of the α-Al matrix and eutectic phase colonies under a load of 0.3 kgf. ST indicates the hardness of the solution-treated state and is arbitrarily positioned at 50 °C.

The large decrease in hardness at temperatures above 200 °C is likely due to coarsening effects of the τ-$Mg_{32}(Al,Zn)_{49}$ phase. Coarsening can only begin after the equilibrium volume fraction has been formed, which means all the solute needed to create the τ-$Mg_{32}(Al,Zn)_{49}$ phase has been removed from the α-matrix. This results in loss of solid solution-strengthening contributions of Mg and Zn in each alloy. Furthermore, coarsening results in an increase in precipitate size and a decrease in the number density of the τ-$Mg_{32}(Al,Zn)_{49}$ phase, which reduces the precipitate-strengthening contributions. Finally, the equilibrium volume fraction of the τ-$Mg_{32}(Al,Zn)_{49}$ phase decreases as the aging temperature increases, as shown by Fig. 13, which further decreases any strengthening contributions of the τ-$Mg_{32}(Al,Zn)_{49}$ phase. The fact that the microhardness measured above 250 °C is greater in the eutectic colonies compared to the α-matrix suggests that coarsening can be limited within eutectic α-Al as the diffusion distance is limited due to constraint of α-Al trapped within $Al_{11}Ce_3$ eutectic lathe spacing. The finer size of the τ-$Mg_{32}(Al,Zn)_{49}$ phase within eutectic α can therefore retain a greater strengthening contribution than the τ-$Mg_{32}(Al,Zn)_{49}$ phase formed in primary α-matrix. Thus, hardness retention may be improved by increasing the total fraction of eutectic $Al_{11}Ce_3$ formation. This may be achieved by increasing the concentration of Ce in the alloy and by decreasing the concentration of Mg and Zn. However, decreasing Mg and Zn can result in a lower precipitation-hardening response.

3.2.2 Dual-Step Aging

The hardness retention of peak aged CMZ764 was evaluated using a dual-step heat treatment of 200 °C for 2 h followed by aging at 315 °C for 1, 2, and 4 h from an initial solution-treated condition (485 °C/2 h). The results shown in Fig. 15 revealed that the peak hardness returns to that of the as-cast and solution-treated states after as little as 1 h at 315 °C and remains constant within error after 4 h. This indicates that while the hardening response of CMZ764 is excellent, the precipitates are not thermally stable and are likely coarsened at 315 °C.

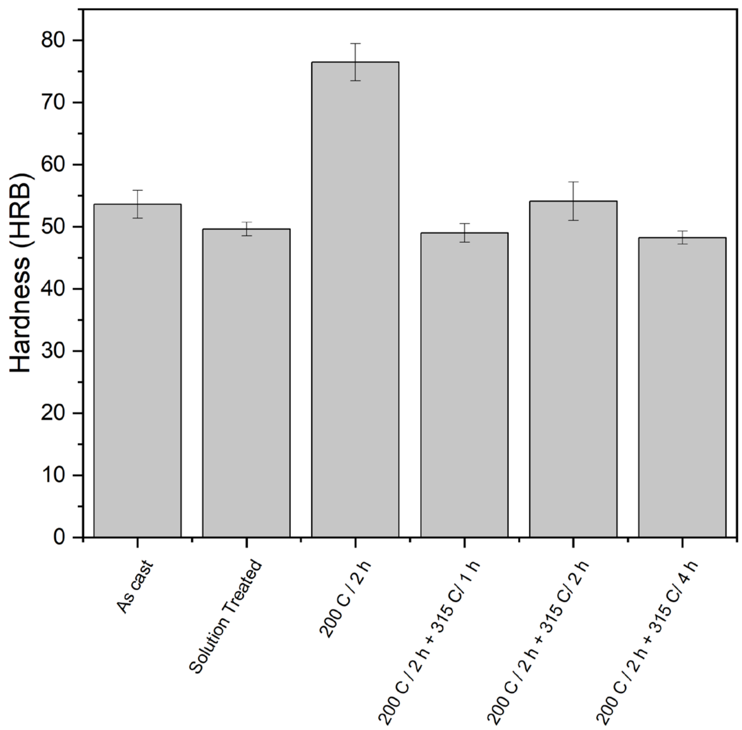

Fig. 15 HRB of CMZ764 alloy samples after dual-step heat treatment to assess hardness retention

3.2.3 Long-Term Aging

The effects of long-term aging of CMZ764 at 315 °C were explored in the as-cast and homogenized states, where homogenization was performed at 485 °C for 2 h and then water quenched before further aging. The change in hardness is shown in Fig. 16a for Rockwell B and Fig. 16b for Vickers microhardness. Vickers hardness measurements were a composite average of the alloy surface with no discrimination between eutectic colonies and the α-Al matrix. For both hardness methods, the greatest hardness was measured in the as-cast and homogenized states with no aging at 315 °C (time = 0 h). The hardness decreased continuously after 200 and 500 h in the homogenized condition, while a decrease in hardness was only measured for the as-cast state after 500 h.

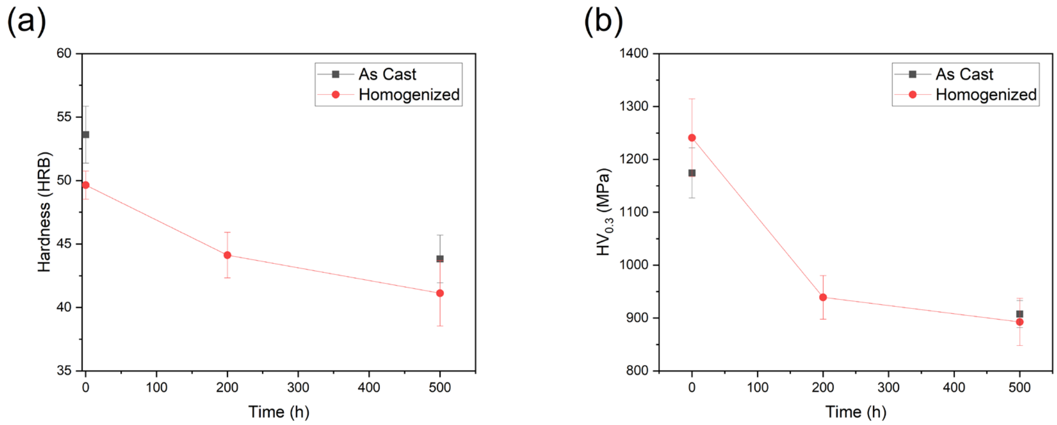

Fig. 16 The change in hardness of CMZ764 in the as-cast and homogenized states at 315 °C up to 500 h. (a) Shows the hardness measured by Rockwell B while (b) shows the hardness measured by Vickers microhardness with a load of 0.3 kgf. Homogenization was performed at 485 °C for 2 h.

Investigation into the cause of the decrease in hardness was performed via BSE imaging. Figure 17 shows characteristic microstructures for CMZ764 in the as-cast state and after homogenization. The as-cast state showed the characteristic Chinese script $Al_{11}Ce_3$ phase and divorced eutectic τ-$Mg_{32}(Al,Zn)_{49}$ phase similar to the CMZ764 button. After homogenization, almost all of the τ-$Mg_{32}(Al,Zn)_{49}$ phase disappeared, indicating dissolution into the α-Al matrix. However, long-term aging at 315 °C for both the as-cast and homogenized states revealed the presence of the coarse τ-$Mg_{32}(Al,Zn)_{49}$ phase (Fig. 18). The coarse τ-$Mg_{32}(Al,Zn)_{49}$ phase is most prominent after 500 h of aging (Figs. 18a and 18c), where it is apparent that τ-$Mg_{32}(Al,Zn)_{49}$ advances from forming a discontinuous layer along grain boundaries after 200 h (Fig. 18b) to a continuous layer after 500 h in the homogenized state; meanwhile, the intragranular τ-$Mg_{32}(Al,Zn)_{49}$ phase can also be observed throughout. Furthermore, the BSE images from 200 to 500 h revealed large coarsening of the τ-$Mg_{32}(Al,Zn)_{49}$ phase, which is likely causing the loss in hardness as Mg and Zn is removed from the α-Al matrix, thus reducing the solid solution-strengthening contribution as discussed in Section 3.2.1. Coarsening of fine nano-sized precipitates that cannot be seen using SEM are also likely reducing the hardness as dislocation bypass becomes the easiest path for dislocation movement.

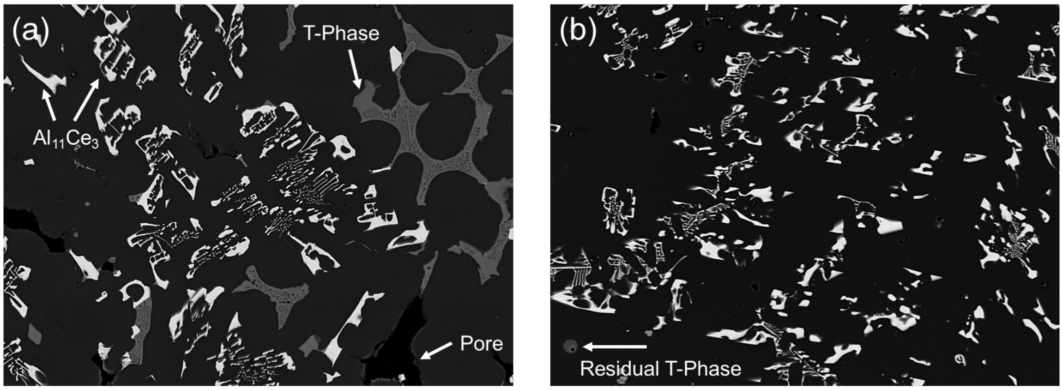

Fig. 17 BSE images of CMZ764 in the (a) as-cast form and (b) after homogenization at 485 °C for 2 h

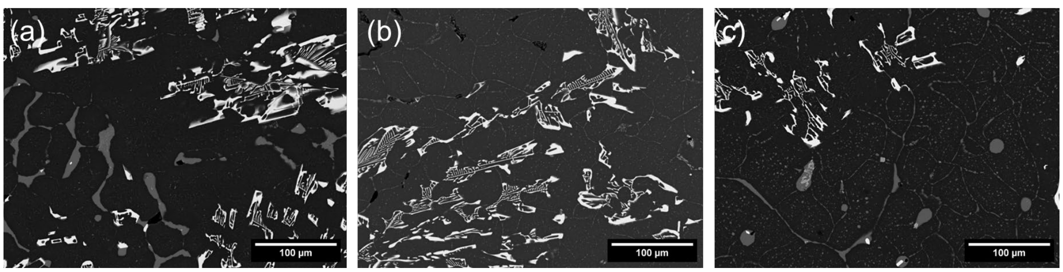

Fig. 18 Characteristic BSE images of CMZ764 in the (a) as-cast form after 500 h at 315 °C and the homogenized form after (b) 200 h at 315 °C and (c) 500 h at 315 °C

3.3 Wedge Melts

A cast wedge of CMZ764 was produced and samples were prepared for tensile testing and evaluation of the coefficient of thermal expansion (CTE) using the cut plan given in Fig. 19. Dog bone flat tensile specimens (Fig. 20) cut from the center line of the wedge were pulled in the as-cast form to assess the effects of solidification rate on tensile behavior. The results for one tensile test at each height of the wedge is shown in Fig. 21 and revealed a very high yield strength (σ_{YS}) and ultimate tensile strength (σ_{UTS}) near the tip of the wedge with a yield strength (YS) of 294 MPa and ultimate tensile strength (UTS) of 395 MPa relative to sand-cast A356.0-T6, which possesses a typical YS of 165 MPa and UTS of 228 MPa at room temperature.[24] However, the yield and tensile strengths rapidly decrease as the solidification rate slows such that both values are below that of A356.0-T6 and the ductility is very low (<2%).

The CTE of CMZ764 in the as-cast condition was determined from linear fitting of the percentage linear change versus temperature from linear dilatometry data collected in Fig. 22. The results show that CMZ764 possessed a larger slope and thus, larger thermal expansion than A356 in the as-cast state. A linear fit of the measured data up to 100 °C provides the best basis of comparison to other cast Al alloys whose data availability beyond 100 °C is scarce. The CTE value that Perrin et al.[22] measured for CMZ764-F was 22.6 μm/m-°C, whereas it was 21.3 μm/m-°C for A356.0-T6, which is in good agreement with the literature value of 21.5 μm/m-°C.[24]

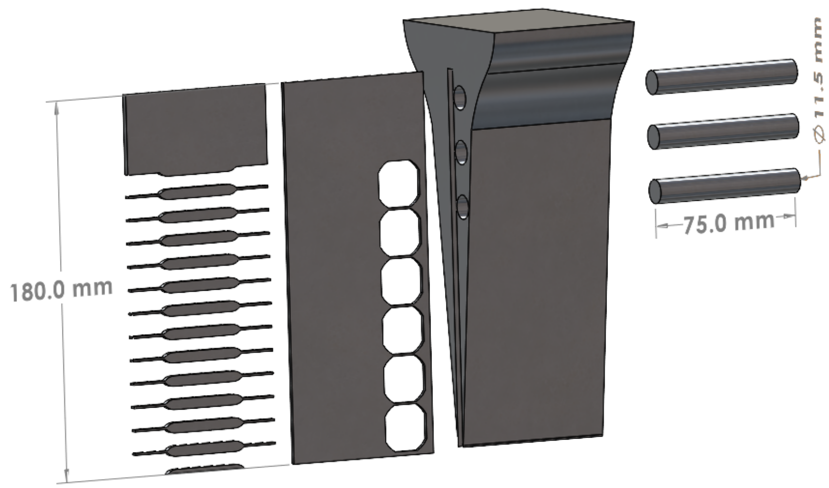

Fig. 19 Test cut plan for CMZ764 wedge analysis. Dog bone tensile specimens, pucks for shear punch testing (not performed), and cylinders for CTE determination are shown.

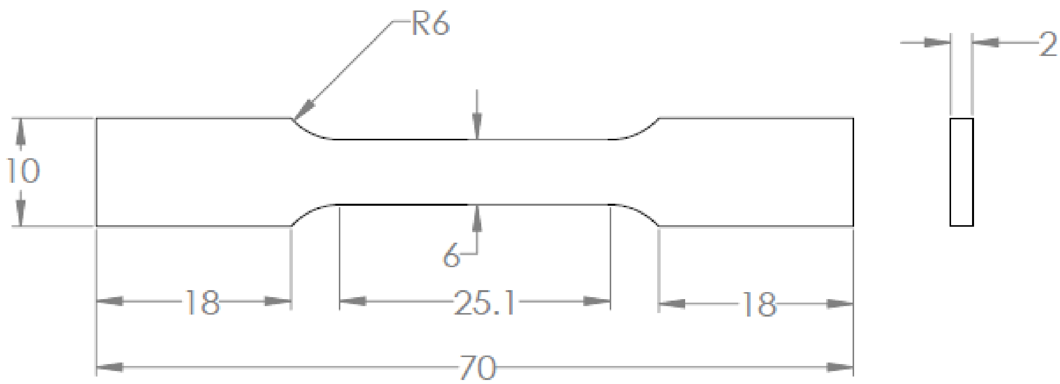

Fig. 20 Schematic drawing of the modified subsize ASTM E8[25] flat dog bone style tensile specimens. The dimensions are in millimeters.

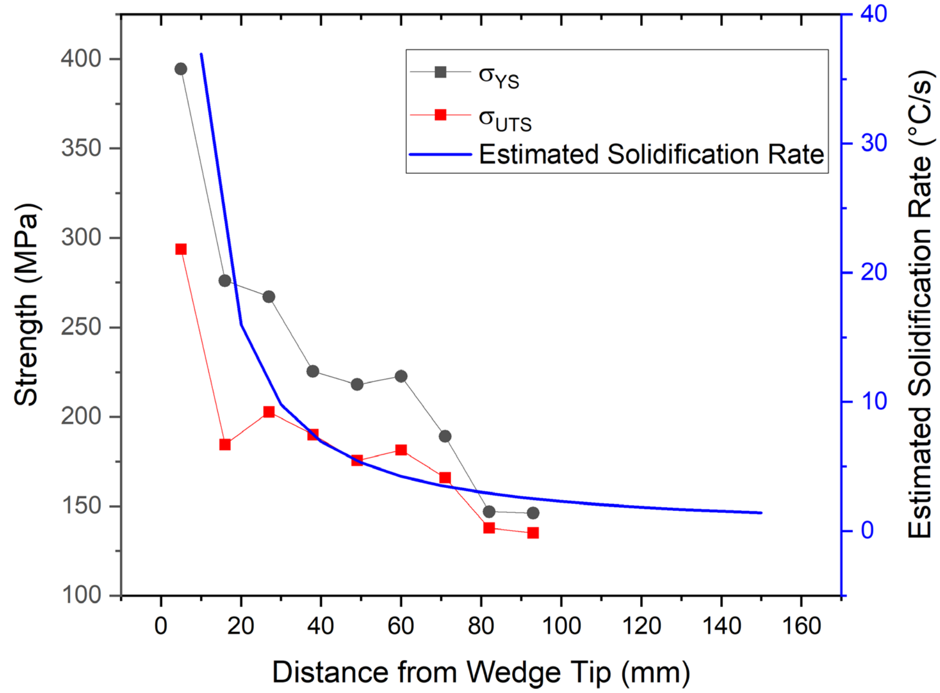

Fig. 21 YS and UTS of the CMZ764 wedge casting as a function of distance from the tip of the wedge. Only one specimen was tested at each data point.

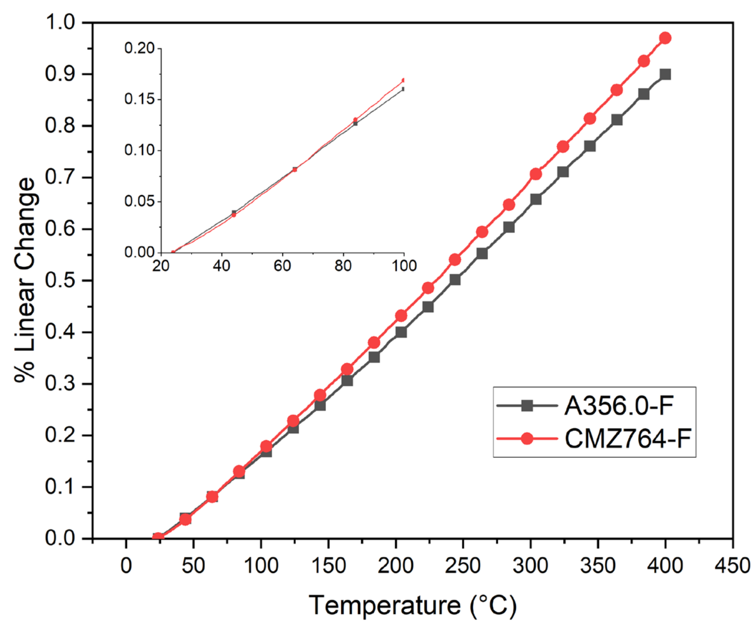

Fig. 22 Percentage linear change as a function of temperature for CMZ764 in the as-cast condition compared to A356.0 in the as-cast state

3.4 The Al–Ce–Mg–Zn Alloy System

The goal of this study was to develop a novel high-performance casting alloy for the replacement of legacy cast-aluminum alloys. The Al–Ce–Mg–Zn alloy system has shown great promise as a precipitation hardenable alloy system. The findings presented here are in agreement with recent studies of wrought Al–Mg–Zn-based alloys strengthened by the τ-$Mg_{32}(Al,Zn)_{49}$ phase whereby a large age-hardening effect has been reported.[26–29] However, the Al–Ce–Mg–Zn did not show good resistance to changes in microstructure and mechanical properties at temperatures above 200 °C, which deems it not suitable for high-temperature applications. Further development of castable Al–Ce–Mg–Zn is recommended for applications below 100 °C as coarsening of the τ-$Mg_{32}(Al,Zn)_{49}$ phase is likely limited and the composition can be tuned for an array of mechanical applications.

4. Conclusions

Cast Al–Ce–Mg–Zn-based alloys have excellent precipitation hardenability due to the likely formation of nano-sized precipitates through natural aging or artificial aging of τ-$Mg_{32}(Al,Zn)_{49}$ phase.

The τ-$Mg_{32}(Al,Zn)_{49}$ phase rapidly coarsens at temperatures above 200 °C, which results in loss in mechanical properties such that the overaged hardness is below that in the as-cast and solution-treated states, indicating that the $Al_{11}Ce_3$ phase and solid solution strengthening are the dominant strengthening mechanisms.

The mechanical properties of an Al–7Ce–6Mg–4Zn alloy are very sensitive to solidification rate given by a 2.5 times decrease in yield and tensile strength from the tip of the wedge casting to the top of the wedge casting suggesting that Al–Ce–Mg–Zn alloys may not provide consistent mechanical properties in thick castings.

5. References

1. Weiss D. Improved high-temperature aluminum alloys containing cerium. J Mater Eng Perform. 2019;28(4):1903–1908.
2. Sims ZC, Weiss D, McCall SK, McGuire MA, Ott RT, Geer T, Rios O, Turchi PA. Cerium-based, intermetallic-strengthened aluminum casting alloy: high-volume co-product development. JOM. 2016;68(7):1940–1947.
3. Stromme ET, Henderson HB, Sims Z, Kesler MS, Weiss D, Ott R, Meng F, Kassoumeh S, Evangelista J, Begley G, et al. Ageless aluminum–cerium-based alloys in high-volume die casting for improved energy efficiency. JOM. 2018;70(6):866–871.
4. Ng DS, Dunand DC. Aging- and creep-resistance of a cast hypoeutectic Al-6.9Ce-9.3Mg (wt.%) alloy. Mater Sci Eng A. 2020;786:139398.
5. Lv H, Peng P, Feng T, Gao H, Ju J, Wang B, Wang J, Sun B. High-performance co-continuous Al–Ce–Mg alloy with in-situ nano-network structure fabricated by laser powder bed fusion. Addit Manuf. 2022;60(A):103218.
6. Rakhmonov JU, Weiss D, Dunand DC. Solidification microstructure, aging evolution, and creep resistance of laser powder-bed fused Al–7Ce–8Mg (wt.%). Addit Manuf. 2022;55:102862.
7. Belov NA, Naumova EA, Eskin DG. Casting alloys of the Al–Ce–Ni system: microstructural approach to alloy design. Mater Sci Eng A. 1999;271 (1–2):134–142.
8. Raghavan V. Al–Ce–Ni (aluminum–cerium–nickel). JPED. 2009;30(3):265–267.
9. Wu T, Plotkowski A, Shyam A, Dunand DC. Microstructure and creep properties of cast near-eutectic Al–Ce–Ni alloys. Mater Sci Eng A. 2022;833:142551.
10. Mondolfo LF. Al–Ce–Mn aluminum–cerium–manganese system. In: Mondolfo LF, editor. Aluminum alloys: structures and properties. Butterworth-Heinemann; 1976. p. 470–471.
11. Coury FG, Kiminami CS, Botta WJ, Bolfarini C, Kaufman MJ. Design and production of Al–Mn–Ce alloys with tailored properties. Mater Des. 2016;110:436–448.

12. Yang Y, Bahl S, Sisco K, Lance M, Shin D, Shyam A, Plotkowski A, Dehoff RR. Primary solidification of ternary compounds in Al-rich Al–Ce–Mn alloys. J Alloys Compd. 2020;844:156048.

13. Farkoosh AR, Dunand DC, Seidman DN. Solute-induced strengthening during creep of an aged-hardened Al–Mn–Zr alloy. Acta Mater. 2021;219.

14. Ekaputra CN, Rakhmonov JU, Senvardarli E, Weiss D, Mogonye J-E, Dunand DC. Combining solution-, precipitation-, and load-transfer strengthening in a cast Al–Ce–Mn–Sc–Zr alloy. Acta Materialia. 2024;266:119683. doi.org/10.1016/j.actamat.2024.119683.

15. Sisco KD, Plotkowski A, Yang Y, Allard L, Fancher C, Rawn C, Poplawsky JD, Dehoff R, Babu SS. Heterogeneous phase transformation pathways in additively manufactured Al–Ce–Mn alloys. J Alloys Compd. 2023;938:168490.

16. Ajantiwalay T, Michi R, Roach C, Shyam A, Plotkowski A, Devaraj A. Influence of microstructural heterogeneities on small-scale mechanical properties of an additively manufactured Al–Ce–Ni–Mn alloy. Addit Manuf Lett. 2022;3.

17. Kozakevich J. Stroh J, Mallouhi V, Sediako D, Weiss D. Interplay between cooling rate, microstructure, and mechanical properties of an Al–Ce–Ni–Mn alloy. Light Met. 2022:83–91.

18. Michi RA, Sisco K, Bahl S, Yang Y, Poplawsky JD, Allard LF, Dehoff RR, Plotkowski A, Shyam A. A creep-resistant additively manufactured Al–Ce–Ni–Mn alloy. Acta Materialia. 2022;227:117699.

19. Emery R, Rios OR, Lass EA, Jorgensen CS, Gilbert DA, Meier WR, Koehler MR, Rack PD. Identification of low coefficient of thermal expansion in Al23Ce4Ni6 via combinatorial sputtering of Al–Ce–Ni–Mn thin films and upscaling to bulk materials. J Alloys Compd. 2023;968:172220.

20. Kozakevich JR, Stroh J, Sediako D, Weiss D. Solidification kinetics of an Al–Ce alloy with additions of Ni and Mn. Metals. 2023;13(5).

21. Michi RA, Simpson JJ, Bahl S, Campbell Q, Brackman P, Plotkowski A, Dehoff RR, Haynes JA, Wang Q, Shyam A. Additively manufactured Al–Ce–Ni–Mn alloy with improved elevated-temperature fatigue resistance. Addit Manuf. 2023;66:103477.

22. Perrin AE, Michi RA, Leonard DN, Sisco KD, Plotkowski AJ, Shyam A, Poplawsky JD, Allard LF Jr, Yang Y. Effect of Mn on eutectic phase equilibria in Al-rich Al–Ce–Ni alloys. J Alloys Compd. 2023;965:171455.

23. Cain T, Mogonye J-E. Method for rapid small-scale simulated aluminum alloy castings. DEVCOM Army Research Laboratory (US); 2021 Nov. Report No: ARL-TN-1091.

24. Anderson K, Weritz J, Kaufman JG, editors. 356.0 and A356.0. In: ASM handbook, vol. 2B: properties and selection of aluminum alloys. ASM Int. 2019;548–552.

25. ASTM E8. Standard test methods for tension testing of metallic materials. ASTM International; 2022.

26. Ding QW, Zhang D, Pan Y, Hou S, Zhuang L, Zhang J. Strengthening mechanism of age-hardenable Al–Mg–3Zn alloys. Mater Sci Technol. 2019;35(9):1071–1080.

27. Pan YL, Zhang D, Liu H, Zhuang L, Zhang J. Precipitation hardening and intergranular corrosion behavior of novel AlMg-Zn(-Cu) alloys. J Alloys Compd. 2021;853:157199.

28. Stemper L, Tunes MA, Dumitraschkewitz P, Mendez-Martin F, Tosone R, Marchand D, Curtin WA, Uggowitzer PJ, Pogatscher S. Giant hardening response in AlMgZn(Cu) alloys. Acta Materialia. 2021;206:116617.

29. Takata N, Takagi R, Li R, Ishii H, Suzuki A, Kobashi M. Precipitation morphology and kinetics of T-AMg11Zn intermetallic phase in Al–Mg–Zn ternary alloys. Intermetallics. 2021;139:107364.

List of Symbols, Abbreviations, and Acronyms

Al	aluminum
Ar	argon
Bal.	balance
BN	boron nitride
BSE	backscattered electron
CAMI	Coated Abrasive Manufacturer's Institute
Ce	cerium
Co	cobalt
CTE	coefficient of thermal expansion
Cu	copper
DEP	divorced eutectic phase
DEVCOM	US Army Combat Capabilities Development Command
EDS	energy-dispersive spectroscopy
He	helium
HRB	hardness Rockwell B
ID	identification
kgf	kilogram force
Mg	magnesium
SEM	scanning electron microscopy
SiC	silicon carbide
UTS	ultimate tensile strength
VH	Vickers microhardness
VIM	vacuum induction melting
wt%	weight percent
XRD	X-ray diffraction
YS	yield strength
Zn	zinc

1 DEFENSE TECHNICAL
(PDF) INFORMATION CTR
DTIC OCA

1 DEVCOM ARL
(PDF) FCDD RLB CI
TECH LIB